Subwavelength multiple topological interface states in one-dimensional labyrinthine acoustic metamaterials

Zhiwang Zhang,[1,2] Ying Cheng,[1,*] Xiaojun Liu,[1,†] and Johan Christensen[2,‡]

[1]*Department of Physics, MOE Key Laboratory of Modern Acoustics, Collaborative Innovation Center of Advanced Microstructures, Nanjing University, Nanjing 210093, China*

[2]*Department of Physics, Universidad Carlos III de Madrid, ES-28916 Leganés, Madrid, Spain*

(Received 8 May 2019; published 26 June 2019)

Acoustic analogies of topological insulators reside at the frontier of ongoing metamaterials research. Of particular interest are the topological interface states that are determined by the Zak phase, which is the geometric phase characterizing the topological property of the bands in one-dimensional systems. Here we design double-channel Mie resonators based on the so-called labyrinth acoustic metamaterials, which can be considered equivalent to a ultraslow medium of large refractive index, inevitably containing structural features on a subwavelength scale. The metamolecule containing two cells is engineered to host the degenerated states through a zone-folding mechanism, whereupon the Zak phase transition takes place when the interval between two cells changes from shrunk to expanded. Furthermore, the topological interface state displays strong robustness against randomly introduced perturbations whose acoustic intensity is enhanced by nearly a factor 1600 in comparison to an ordinary waveguide.

DOI: 10.1103/PhysRevB.99.224104

I. INTRODUCTION

The hallmark of topological insulators is wave propagation and guiding in the absence of back-scattering by means of exotic surface and edge-state excitation [1,2]. Therefore it was no surprise that this line of research took the realm of classical physics such as optics [3–7], acoustics [8–20] and mechanics [21–25] by storm. A celebrated and simple implementation is the one in one-dimensional (1D) periodic system whose topological properties are determined by the Zak phase [26], which has been explored in a palette of exciting classical realizations [27–33]. Specifically, in acoustics, such Zak system was proposed for the first time in a cylindrical waveguide with periodically alternating cross sections hosting topological interface states and has ever since been extended for further studies [29–31].

On the other hand, acoustic metamaterials [34] are artificially designed to control and manipulate sound waves to obtain unprecedented wave phenomena such as negative refraction [35], sound collimation [36], and holography [37,38]. Specifically, artificial Mie resonators, which can be equivalently constructed out of an ultraslow medium, have been realized with the aim to tailor extraordinary sound transmission and absorption [39–41].

In this work, we present a 1D phononic crystal (PnC) containing Mie resonators to facilitate a subwavelength topological system [42] within an ordinary straight acoustic waveguide, which differs substantially from previous designs that are based on geometrical modulations of the waveguide itself [29–31]. Quantitatively we are able to calculate the Zak phase to define the topological characteristics of band structures, which are induced by the multipolar Mie resonances. Hence, as opposed to the conventional geometrical phase modulations of the basic waveguide geometry, topological band inversion is readily possible by displacing the resonators, i.e., changing the interval among neighboring unit cells. This flexible mechanism to tune Zak phases also appears to be highly robust against different kind of perturbations such as displacement of the resonator chain. The existence of the interface states in each band gap is verified through calculated eigenfrequency and detected pressure spectra. Also, the intensity enhancement and the spatial confinement are discussed in detail. Furthermore, the proposed 1D PnC structures promise good flexibility in real applications because of its strong durability against variations of the Mie resonator sites and against the deformation of the acoustic waveguide.

II. RESULTS AND DISCUSSION

A. Structure of Mie resonator

We design a double-channel Mie resonator (DMR) based on the cylindrical labyrinthine acoustic metamaterials, whose cross-sectional view is shown in Fig. 1(a). The single DMR is composed of two identical semicircular parts and each part consists of a meander channel with a rigid wall thickness $t = 1$ mm and a slit width $w = 2.5$ mm. The inner radius of the DMR is $R_i = 4$ mm and the outer radius is defined by $R_o = R_i + N(t + w) + t$, with N the curling number that is chosen as $N = 8$ in this work. The propagation length of sound waves into DMR is thus multiplied after introducing the aforementioned meander channel. As a result, the size of the unit cell can be designed on the subwavelength scale [39,41].

*chengying@nju.edu.cn
†liuxiaojun@nju.edu.cn
‡johan.christensen@uc3m.es

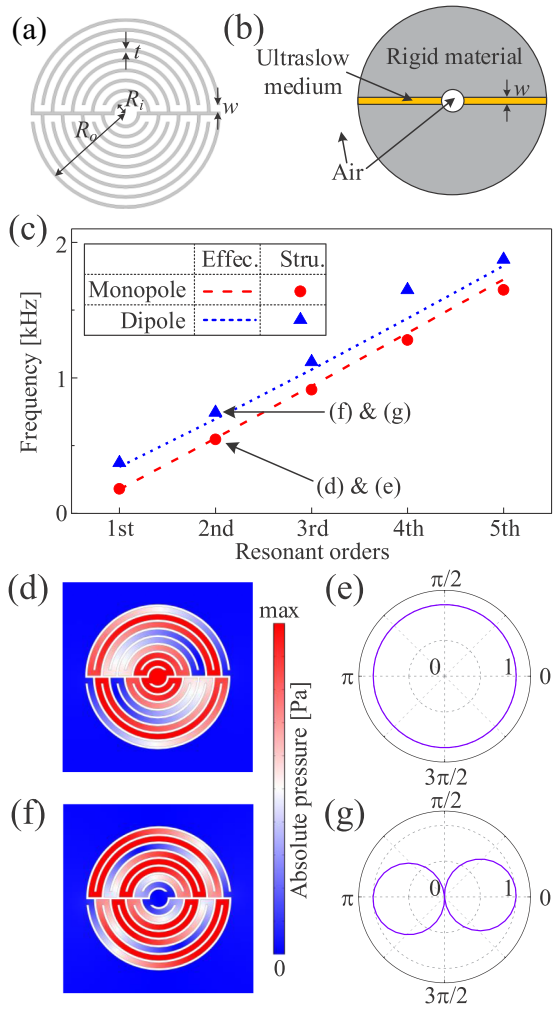

FIG. 1. Schematic of (a) the structural model and (b) the effective medium of a DMR. (c) Resonant frequencies of the multiorder monopole and dipole states. Red dashed and blue dotted lines represent the monopole and dipole states with the effective medium, respectively. Red circles and blue triangles represent the results with structural model. (d) Distributions of the absolute pressure fields and (e) the far-field patterns of the second-order monopole state. (f)–(g) Same as (d)–(e) but of the second-order dipole state.

Additionally, we demonstrate that the DMR is equivalent to an effective medium as shown in Fig. 1(b), which consists of a perforated rigid cylinder connecting two straight channels of ultraslow medium. The velocity and mass density of air are $c_0 = 343$ m/s and $\rho_0 = 1.21$ kg/m^3, respectively. The effective refractive index of the ultraslow medium can be defined as $n_r = L_p/[2(R_o - R_i)]$ with L_p the total propagation lengths in the DMR, which can be calculated as

$$L_p = \sum_{n_i=1}^{N} 2\pi[R_i + n_i(t + w) - w] - 2Nw. \quad (1)$$

Consequently, the effective refractive index here is $n_r = 14.3$. To verify the designed model, the calculated eigenfrequencies of the multiorder monopolar and dipolar states in the structural model and the effective medium are illustrated in Fig. 1(c), from which the good agreement between these two models

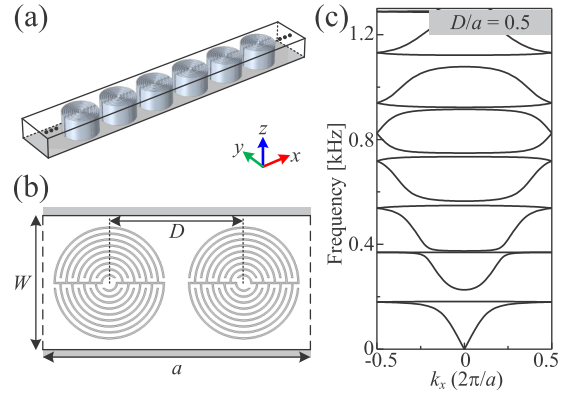

FIG. 2. (a) Schematic of the one-dimensional phononic crystal based on a DMR chain in a 1D acoustic waveguide. (b) Schematic of the metamolecules containing two DMRs with the lattice constant a. The distance between two subcells in the metamolecule and the width of the waveguide are labeled as D and W, respectively. (c) Band diagram of the PnC with $D/a = 0.5$, from which the doubly degenerated points can be obtained at the boundary of the first Brillouin zone (BZ) due to the zone folding effect.

can be inferred. The finite-element software COMSOL MULTIPHYSICS is utilized in the simulations. Note that there only exist monopolar and dipolar states due to the designed double-channel structure. To clearly demonstrate the resonant nature, the absolute pressure distributions, and the corresponding far-field patterns of the second-order monopolar states and dipolar states in structural DMR are illustrated in Figs. 1(d)–1(e) and Figs. 1(f)–1(g), respectively. The corresponding eigenmodes of the effective medium are discussed in Appendix A.

B. Topological phase transition

As shown in Fig. 2(a), the 1D PnC composed of DMR chain is embedded in a 1D acoustic waveguide. Figure 2(b) illustrates the detailed geometric parameters of the metamolecule containing two DMRs. The band diagram of the unperturbed PnC with resonator ratio $D/a = 0.5$ is illustrated in Fig. 2(c), which agrees well with the band diagram of the PnC composed of effective medium cylinders (see Appendix B). In the simulations, the Floquet boundary conditions are used at the periodic interfaces between the metamolecules, which are indicated by black dashed lines in Fig. 2(b). Several doubly degenerated states near the eigenfrequencies of the multiorder resonances of DMR can be observed at the boundary of the first BZ, which result from folding the band diagram of the primitive unit cell containing one DMR [11].

Next, the perturbation is introduced to lift the double degeneracies at the folding point by changing the interval between two DMRs in the metamolecule. First, we compute the band diagram for a PnC of shrunken metamolecules with $D/a = 0.45$ and also present the expanded system with $D/a = 0.55$, which are presented in Fig. 3(a) and Fig. 3(d), respectively. We demonstrate that all the degeneracies are lifted in both situations, however, it appears that only the branches between the seventh and the twelfth bands, reopen wide enough to be clearly observable. Therefore, we present an expanded view of the dispersion relations of these bands as

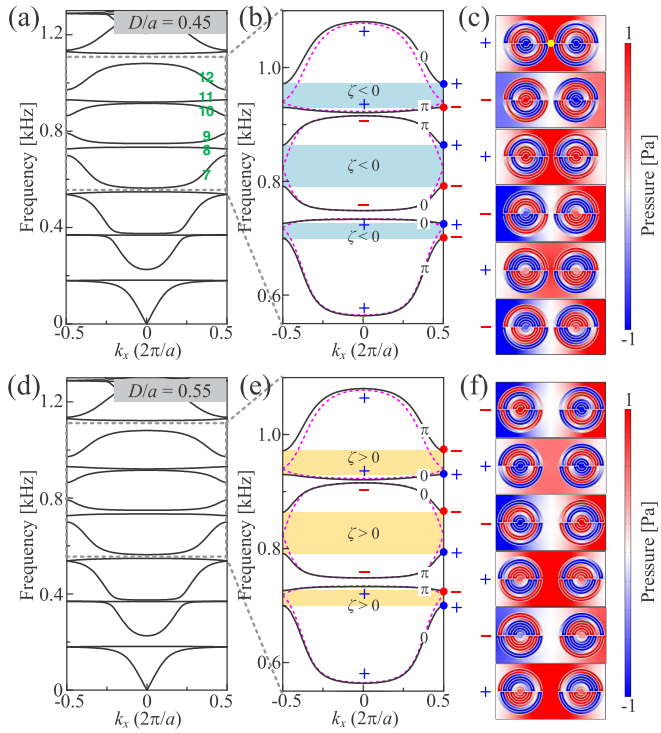

FIG. 3. (a) Band diagram of the PnC composed of the shrunken metamolecule with $D/a = 0.45$. (b) Enlarged view of the dispersion relations in the frequency range indicated in (a). The magenta dashed curves represent the corresponding band diagram of the unperturbed PnC ($D/a = 0.5$). The Zak phase of each band has been labeled. (c) Corresponding eigenmodes of the seventh ∼ twelfth bands at the 1st BZ boundary from bottom to top. (d)–(f) Same as (a)–(c), but for the expanded metamolecule with $D/a = 0.55$. The cyan/yellow regions in (b) and (e) represent band gaps with negative/positive sign of ζ.

shown in Figs. 3(b) and 3(e), respectively. The corresponding pressure distributions of the eigenmodes at the boundary of the first BZ with $k_x = \pi/a$, are accordingly mapped in Fig. 3(c) and Fig. 3(f). Similarly, we present the eigenmodes at the BZ center in the Appendix C. Note that the red dotted eigenmodes have an odd parity (−), while the blue dotted ones have an even parity (+). The odd/even parities at high symmetry points are denoted by the red/blue colored "−/+" in Figs. 3(b) and 3(e). The Zak phase θ of each band is connected with the parities of the eigenmodes according to [26,27,43]

$$\frac{\theta}{\pi} = \frac{1}{2}\left[\eta(k_x = 0) - \eta\left(k_x = \frac{\pi}{a}\right)\right] : \text{modulo } 2, \qquad (2)$$

where η is the parity at different symmetry point. Note that the value of the Zak phase depends on the choice of the integral origin [26,27]. Here Eq. (2) can be utilized to obtain the quantized Zak phase 0 or π when the origin is chosen to be the center of the metamolecule as marked by a yellow dot in Fig. 3(c). As seen in the bands of Fig. 3(b) and Fig. 3(e), the calculated Zak phase from Eq. (2) has been labeled on each band. Although the band diagrams of the shrunk and expanded configurations share the same shape around the three reopened gaps, both the parities of the band-edge eigenmodes and the Zak phases are inverted, which corresponds to a topological phase transition. It has been demonstrated [27] that the topological properties of the bulk dispersion are related to $\zeta^{(n)}$. The sign of $\zeta^{(n)}$ for the nth band gap can be defined by the following relation comprising the discrete Zak phases [27,28]

$$\text{sgn}[\zeta^{(n)}] = (-1)^{n+1}\exp\left(i\sum_{m=1}^{n}\theta_m\right). \qquad (3)$$

Besides the definition in Eq. (3) there is another method to obtain the sign of $\zeta^{(n)}$, which is determined by the parities of the band-edge eigenmodes [27,28]. Interestingly, the band-edge states with odd parity possess zero pressure field at the center of the metamolecule, while those states with even parity contain a pressure maximum. As a result, the sign of $\zeta^{(n)}$ will be negative if the lower edge of the band gap has odd parity and the upper edge has even parity. Otherwise, the sign will be positive. As can be seen in Fig. 3(b), those three band gaps (cyan) of the shrunken metamolecule with $D/a = 0.45$, all have negative signs $\zeta < 0$. On contrary, when the perturbation is introduced by expanding the distance to $D/a = 0.55$, these band gaps (yellow) have a positive sign $\zeta > 0$, as shown in Fig. 3(e).

C. Topological interface state and its robustness

The existence of topological interface states is guaranteed by the condition [27] $\zeta_+ + \zeta_- = 0$, which means the topological phases of the overlapped band gaps of jointed PnCs must be inverted. Based on the above condition, a one-dimensional topological insulator with a interface between two PnCs is designed as shown in Fig. 4(a), which consists of ten metamolecules with $D/a = 0.45$ and ten metamolecules with $D/a = 0.55$ on either side. Figure 4(b) illustrates the calculated eigenfrequencies of the sample described in Fig. 4(a). In the simulations, top and bottom boundaries are set as rigid walls whereas the remaining other two boundaries are set to radiate. As predicted, there exists a single interface state in each band gap. In addition, the values of the absolute pressure are detected at the interface between two PnCs as shown in Fig. 4(c). A source with the amplitude 1 Pa radiates plane waves from left to right side. As can be observed, in each gap, the localized interface state gives rise to a peak (red dots), of which the frequency is identical to the eigenfrequency of the topological interface state in Fig. 4(b). The distributions of pressure fields at frequency $f = 824.3$ Hz, which is in the band gap, is illustrated on the top panel of Fig. 4(c). For comparison, a contrast sample with the trivial band gaps not supporting the interface states is also discussed in Appendix D. We emphasize on two key findings: (i) The sound intensity of the topological state at the interface is enhanced dramatically. As shown in Fig. 4(d), we compute $\beta = I_{\text{topo.}}/I_{\text{ord.}}$ to quantify the enhancement factor of the sound intensity of the topological interface state $I_{\text{topo.}}$ as compared to the intensity of an empty ordinary waveguide $I_{\text{ord.}}$ when probed at the same position. An impressive enhancement factor of nearly 1600 has been predicted in Fig. 4(d). The frequency range is chosen as the second band gap from 791.2 Hz ∼ 863.9 Hz. (ii) Figure 4(e) shows the normalized sound intensity distributions in close proximity to the rigid upper wall in Fig. 4(c), which

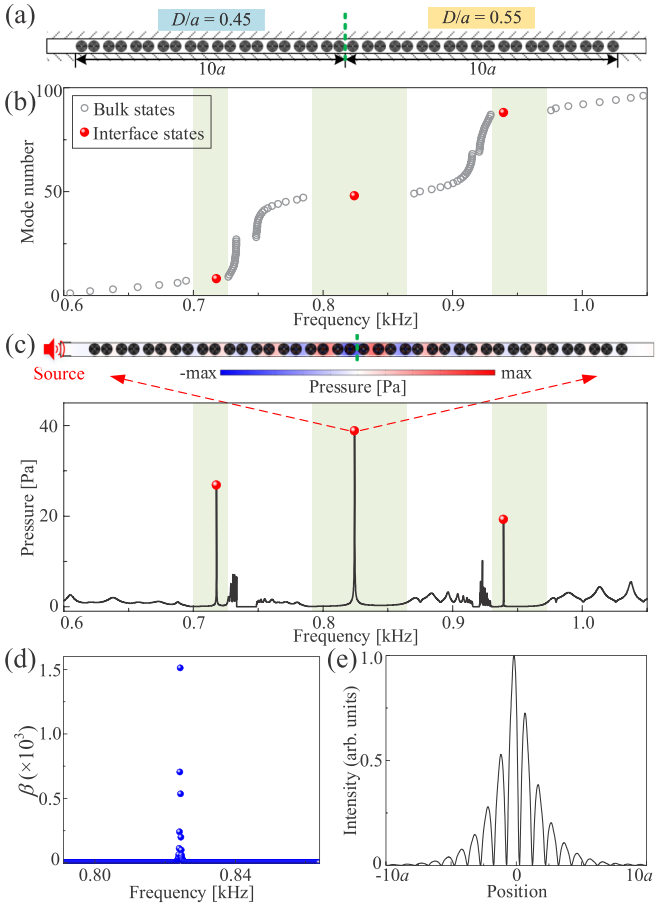

FIG. 4. (a) Schematic of a ribbon-shaped PnC composed of ten metamolecules with $D/a = 0.45$ and ten metamolecules with $D/a = 0.55$ on either side, of which the interface is labeled as green dashed line. (b) Eigenfrequency spectra of the ribbon-shaped PnC. Gray circles and red dots denote the bulk and topological interface states, respectively. Shadowed regions indicate the band gaps in Fig. 3. (c) Absolute pressure detected at the interface between two PnCs. (d) Ratio (β) of the probed sound intensity in the topological interface state ($I_{\text{topo.}}$) to which in the ordinary waveguide without PnC ($I_{\text{ord.}}$). (e) Normalized spatial profile of the sound intensity field for the interface state along the top wall of the waveguide at $f = 824.3$ Hz.

illustrates that the sound energy is concentrated tightly at the interface ($x = 0$) from which it exponentially decays along the x direction. We also demonstrate that considering the acoustic-solid interaction in air instead of the prefect rigid walls, the topological interface states in the proposed structure still exist (see Appendix E). The influence of the thermoviscous losses on the material performance is also discussed in Appendix F. This topologically induced and highly localized acoustic state could, thanks to its prominent acoustic enhancement factor find use in biomedical sound focusing and particle manipulation.

The robustness against defects is the hallmark physical property of the topological states. In order to confirm the robustness of the topological interface states in the 1D PnC, we deliberately introduce disorder through changing the positions of the DMRs as shown in Fig. 5(a). In the left-side sample, the

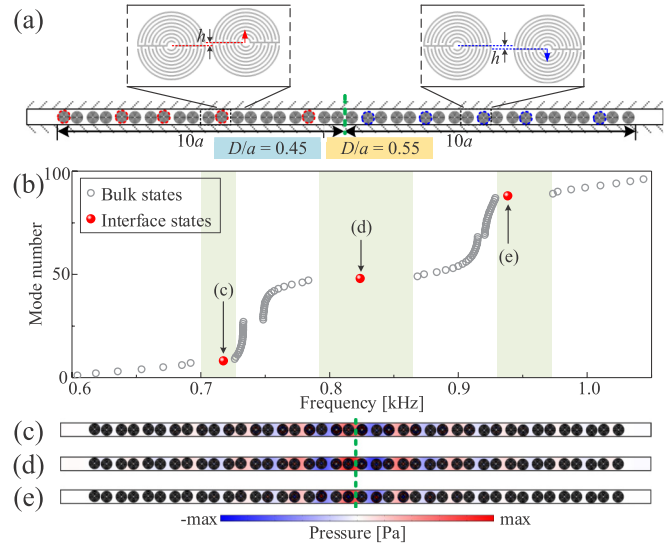

FIG. 5. (a) Topological states in the presence of randomly introduced vertical displacements of the DMRs. As indicated above, we have introduced both an upward- (red) and a downward-going (blue) displacement of distance $h = 0.02a$. (b) Eigenfrequency spectra of the ribbon-shaped PnC with the aforementioned defects. (c)–(e) Acoustic eigenmodes profiles of the interface states after introducing defects as marked by red dots in (b).

randomly chosen DMRs are moved h upwards as compared to their original positions, whereas in the right-side structure we randomly displace the DMRs to the opposite direction, i.e., downwards. At both sides of the topological insulators, although random, the displacements are of uniform value, $h = 0.02a$. We emphasize that the topological interface states still exist in the band gaps even when disorder is introduced, which can be observed from the calculated eigenfrequency spectrum shown in Fig. 5(b). The eigenmodes profiles of the interface states in each band gap are illustrated in Figs. 5(c)–5(e), respectively, depicting how these topological states despite disorder remain entirely localized at the interface. The absolute interface pressure is enhanced with a factor 40, underlining that disorder also has zero influence on the level of confinement strength (see Appendix G). Furthermore, we demonstrate that the DMR crystal is also resilient to any influence of the shape of the waveguide (see Appendix H), which should make such system highly flexible for real world applications.

III. SUMMARY

In conclusion, we have demonstrated multipole topological interface states in a 1D phononic crystal composed of subwavelength DMRs based on labyrinthine acoustic metamaterials. By merging metamaterials and topological insulators into one unit, we have been able to fully characterize the topological band gaps as induced by multipolar Mie resonances via the Zak phase. Beyond unprecedented field enhancements and strong localization we illustratively depict how deep subwavlength resonances, via their topology can constitute highly flexible and robust acoustic guides for the future.

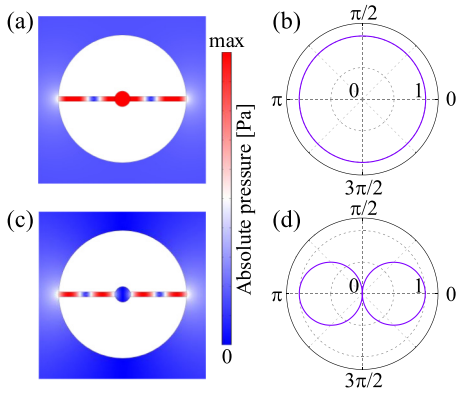

FIG. 6. (a) Distributions of the absolute pressure fields and (b) the far-field patterns of the second-order monopolar state. (c)–(d) Same as (a)–(b) but of the second-order dipolar state.

ACKNOWLEDGMENTS

This work was supported by National Key R&D Program of China (2017YFA0303702), NSFC (11834008, 11874215, 11674172, and 11574148), Jiangsu Provincial NSF (BK20160018), the Fundamental Research Funds for the Central Universities (020414380001) and Nanjing University Innovation and Creative Program for PhD candidate (CXCY17-11). Z.Z. acknowledges the support from the China Scholarship Council. J.C. acknowledges the support from the European Research Council (ERC) through the Starting Grant No. 714577 PHONOMETA and from the MINECO through a Ramón y Cajal grant (Grant No. RYC-2015-17156).

APPENDIX A: SECOND-ORDER MONOPOLAR AND DIPOLAR EIGENMODES OF THE EFFECTIVE MEDIUM

As demonstrated in the main text, a DMR can be treated equivalent to the effective medium. To further verify the good agreement between the effective medium and the DMR, the absolute pressure distributions and the corresponding far-field patterns of the second-order monopolar and dipolar states are illustrated in Fig. 6. Sound energy of the monopole is concentrated at the center of the structure, and radiates equally in all directions, which can be seen in Figs. 6(a)–6(b). However, in the acoustic dipole mode shown in Figs. 6(c)–6(d), sound energy in the structural center is zero and sound radiates along the horizontal plane, i.e., the dipolar axis.

APPENDIX B: BAND DIAGRAM OF THE PnC COMPOSED OF THE EFFECTIVE MEDIUM

Figure 7(a) illustrates the metamolecule of 1D PnC composed of the effective medium with $D/a = 0.5$ and the corresponding band diagram is shown in Fig. 7(b). The doubly degenerated states at the BZ boundary can be achieved through zone folding. It should be noted that the eigenfrequencies of the degenerated states are almost identical to those calculated from the 1D PnC composed of DMRs in the main text, which further verifies the good agreement between the two models.

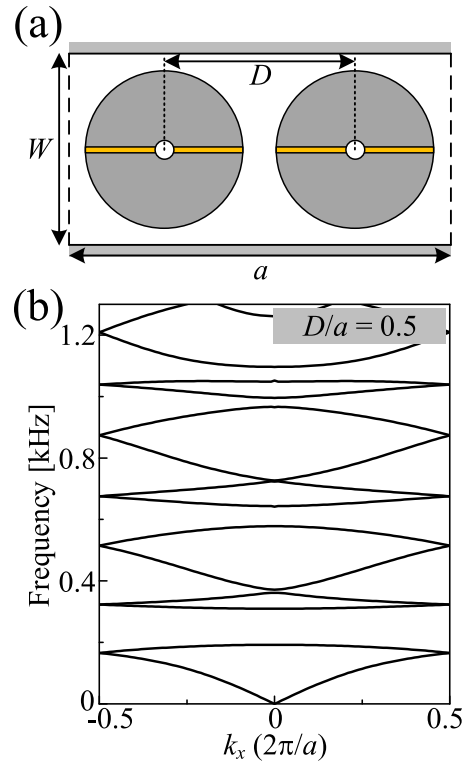

FIG. 7. (a) Schematic of the metamolecule containing two effective medium resonators. (b) Corresponding band diagram of the 1D PnC with $D/a = 0.5$.

APPENDIX C: CORRESPONDING EIGENMODES AT THE BZ CENTER

We demonstrate that the Zak phase θ of each band can be calculated with the parities of the eigenmodes at different points $\eta(k_x = 0)$ and $\eta(k_x = \pi/a)$ according to Eq. (2) in the main text. The eigenmodes at the BZ boundary have been computed in the main text. Here, Fig. 8 shows the corresponding pressure distributions of the eigenmodes at the BZ center where $k_x = 0$, from which the parities can be obtained.

APPENDIX D: A CONTRAST SAMPLE WITH TRIVIAL BAND GAPS

For comparison, a contrast sample composed of ten metamolecules with $D/a = 0.45$ and ten metamolecules with $D/a = 0.44$ on either side is constructed as shown in Fig. 9(a), whose band gaps all have negative values of ζ. As a result, all the band gaps are topological trivial. Figure 9(b) illustrates the eigenfrequency spectra of the sample without interface states to be found in the band gaps. As verified by the detected pressure spectra shown in Fig. 9(c), the flat response in the shaded regions indicates the absence of topological interface states in these trivial band gaps.

APPENDIX E: CONSIDERING THE ACOUSTIC-SOLID INTERACTION

Considering the acoustic-solid interaction in air, the simulations are recalculated in the acoustic-structure interaction

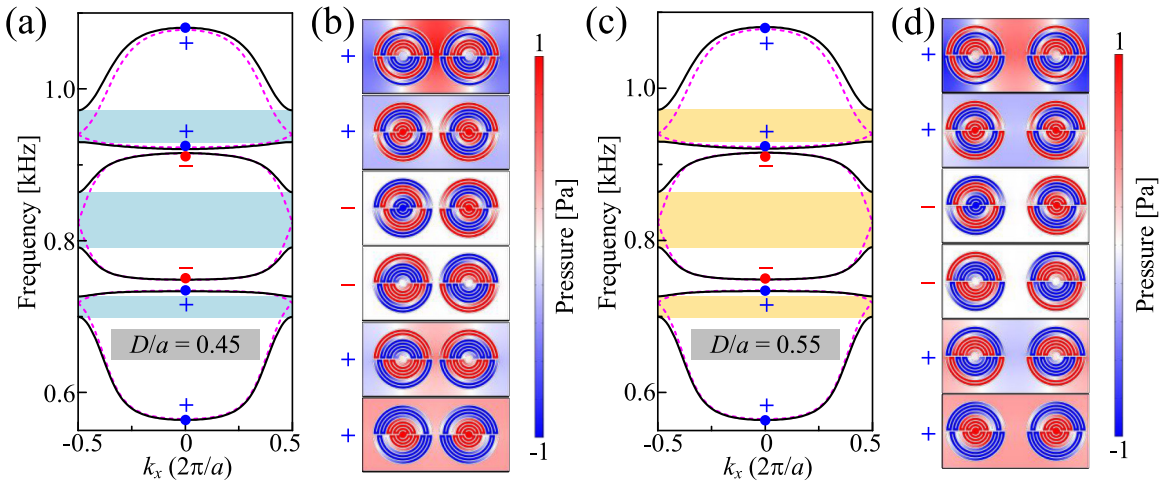

FIG. 8. (a) Dispersion relations of the 1D PnC with $D/a = 0.45$. (b) Corresponding eigenmodes at the BZ center from bottom to top. (c)–(d) Same as (a)–(b), but for the expanded metamolecule with $D/a = 0.55$.

section of the finite-element software COMSOL MULTIPHYSICS. In the simulations, the rigid material is replaced by the steel, of which the mass density, Poisson's ratio and the Young's modulus are $\rho = 7800\ \mathrm{kg/m^3}$, $\nu = 0.3$ and $E = 2.1 \times 10^{11}$ Pa, respectively. As shown in Fig. 10(a), the degeneracy at the BZ boundary is still lifted after expanding/shrinking the distance between two DMRs in the unit cell. The existence of the topological interface state is also verified by the detected pressure amplitude at the interface between two PnCs as shown in Fig. 10(b), which also reaches about 40 similar to the situation with the rigid materials in Fig. 4(c). From the distributions of the pressure fields at the frequency of the interface state, which is illustrated in Fig. 10(c), the energy is confined at the interface. To conclude, the existence of the topological interface states based on the proposed labyrinthine acoustic metamaterials in air will not be influenced if the perfectly rigid material is interchanged with steel. However, it must have serious impact on the physics in the proposed labyrinthine acoustic metamaterials if the background media

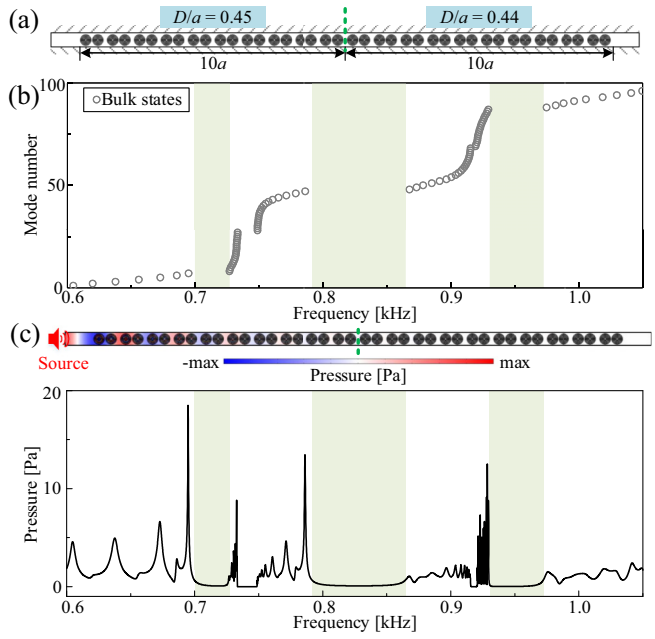

FIG. 9. (a) Schematic of a ribbon-shaped PnC composed of ten metamolecules with $D/a = 0.45$ and ten metamolecules with $D/a = 0.44$ on either side. (b) Eigenfrequency spectra of this ribbon-shaped PnC. (c) Absolute pressure detected at the interface of two PnCs described in (a).

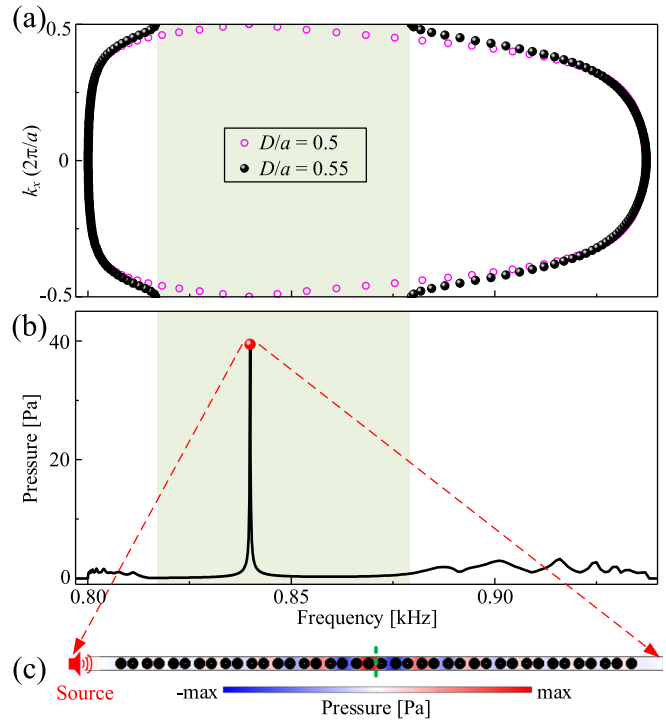

FIG. 10. (a) Partial band diagram of the PnC calculated in the acoustic-structure interaction section. The structure of the PnC is identical as that in FIG. 4(a). (b) Absolute pressure detected at the interface between two PnCs. (c) Distributions of the total pressure fields at the frequency of the topological interface state labeled as red dot in (b).

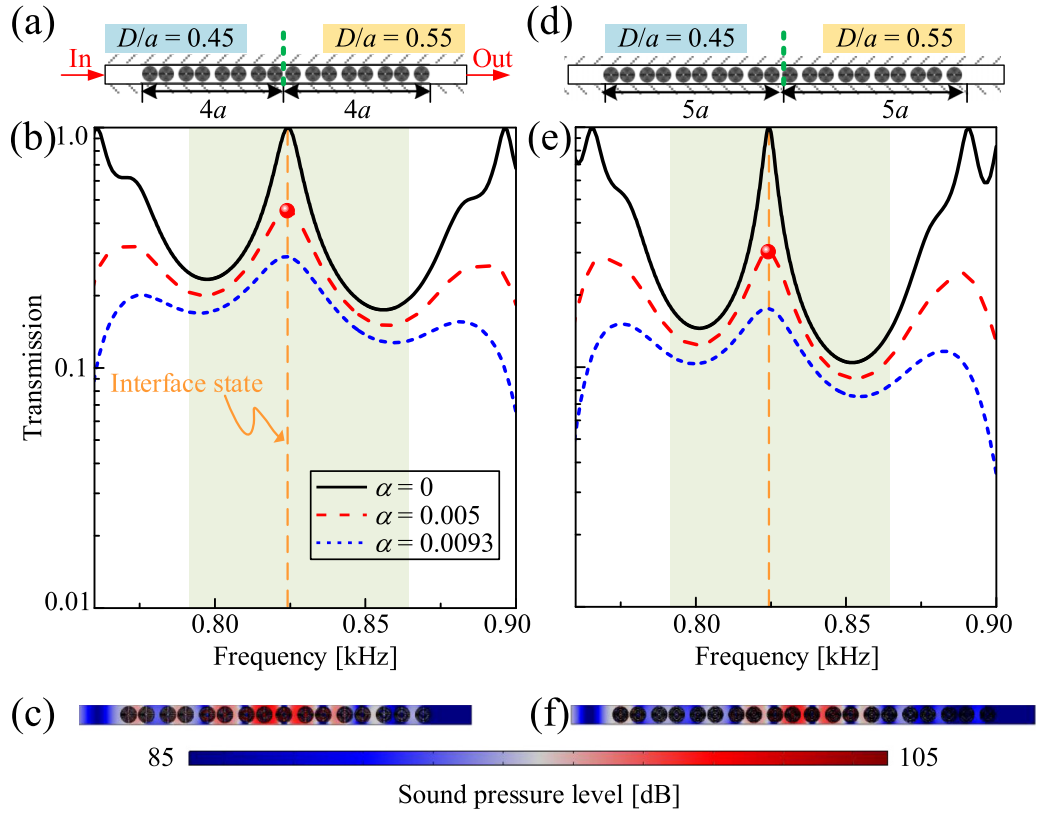

FIG. 11. (a) Schematic of a ribbon-shaped PnC composed of four metamolecules with $D/a = 0.45$ and four metamolecules with $D/a = 0.55$ on either side. (b) Transmission spectra, which are calculated as the ratio between the output and input amplitude, for the situations with the loss coefficient $\alpha = 0$ (black solid curve), $\alpha = 0.005$ (red dashed curve), and $\alpha = 0.0093$ (blue dotted curve), respectively. Shadowed region represents the topological band gap and the orange dashed line marks the corresponding eigenfrequency of the interface state. (c) Corresponding distributions of the sound pressure level at the point labeled as a red dot in (b) with $\alpha = 0.005$. (d)–(f) Same as (a)–(c), but the ribbon-shaped PnC is composed of five metamolecules with $D/a = 0.45$ and five metamolecules with $D/a = 0.55$ on either side.

is the heavy fluid, such as water. Because the incoming wave in water can deform the walls and induce vibrations into the systems, the overall physical picture will inevitably get much more complex. The applications of the labyrinthine acoustic metamaterials in water thus is highly important in future studies not addressed in our paper.

APPENDIX F: INFLUENCE OF THE THERMOVISCOUS LOSSES

The viscous and thermal losses induced by near-wall viscosity and thermal conduction effect should be significant when acoustic waves propagate through channels in the labyrinthine acoustic metamaterials [39]. Considering the influence of the thermal conduction effect, the loss is added into the wave number as

$$k_0 = \frac{2\pi f(1 - i\alpha)}{c_{\text{air}}}, \tag{F1}$$

where α is the attenuation coefficient. In Ref. [39], the attenuation coefficient $\alpha = 0.0093$ is considered in the simulations, which showed good agreement with experiments. Note that the attenuation coefficient depends on the different experimental environment and the materials used in the experiments. The attenuation coefficient can be reduced to a smaller value, such as 0.005, if the experimental environment is optimized.

Figure 11 illustrate the influence of the thermoviscous losses in the proposed systems. Figure 11(a) shows the structure of the 1D PnC composed of eight metamolecules and the calculated transmission is illustrated in Fig. 11(b). We demonstrate that the topological interface state still exists although the thermoviscous losses reduce the transmissions of the interface state and bulk states at the same time. The sound pressure level at the frequency of $f = 824.1$ Hz with $\alpha = 0.005$ shown in Fig. 11(c) further verifies the presence of the interface state even when the thermoviscous losses are considered. Figures 11(d)–11(f) illustrate the situation in the 1D PnC composed of two more metamolecules compared with the former situation. Calculated transmission spectrum in Fig. 11(e)

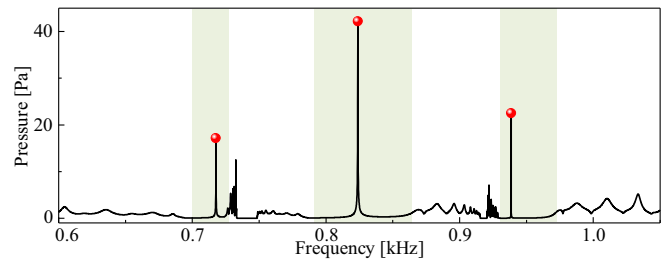

FIG. 12. Absolute pressure detected at the interface between two PnCs with the randomly introduced disorders.

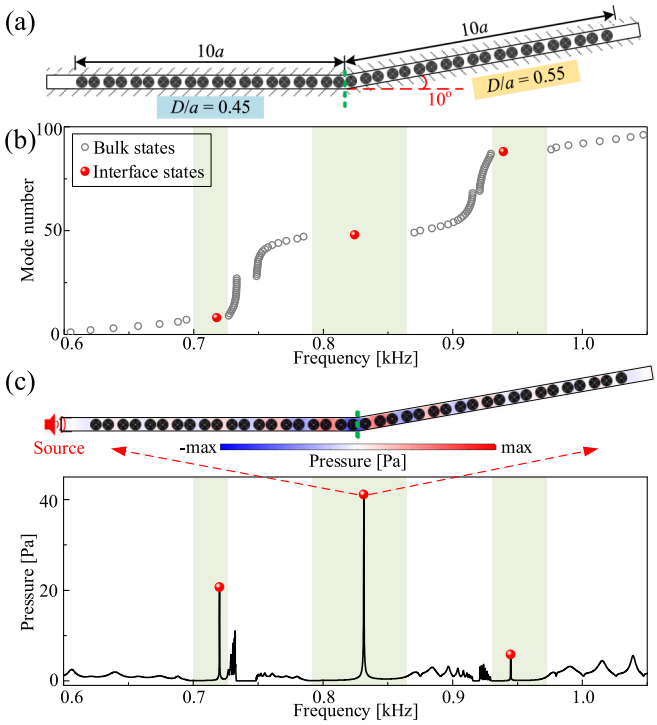

FIG. 13. (a) Rotating one-half of the PnC by 10°. (b) Eigenfrequency spectra of the 10°-bent PnC. (c) Absolute pressure detected at the interface. Top: distributions of the pressure fields with the frequency $f = 831.5$ Hz as labeled by the red dashed line.

demonstrates that the transmitted energy is reduced as a result of the increased transport paths for the sound waves in the DMRs. However, the topological interface state still can be clearly observed. Here we demonstrate that there is a tradeoff between the subwavelength properties and the thermoviscous losses induced by the labyrinthine acoustic metamaterials.

APPENDIX G: DETECTED PRESSURE AT THE INTERFACE IN THE SYSTEM WITH DISORDER

In the system with the randomly introduced disorder, the absolute pressure is detected at the interface as shown in Fig. 12. Note that the interface states still exist as indicated by red dotted peaks with the negligible frequency shift compared to ordered resonators. Moreover, the enhancement factor of the topological interface state also reaches about 40, which is identical to the unperturbed system. As a result, the convincing robustness of the proposed topological interface states against defects in the form of disorder is further verified.

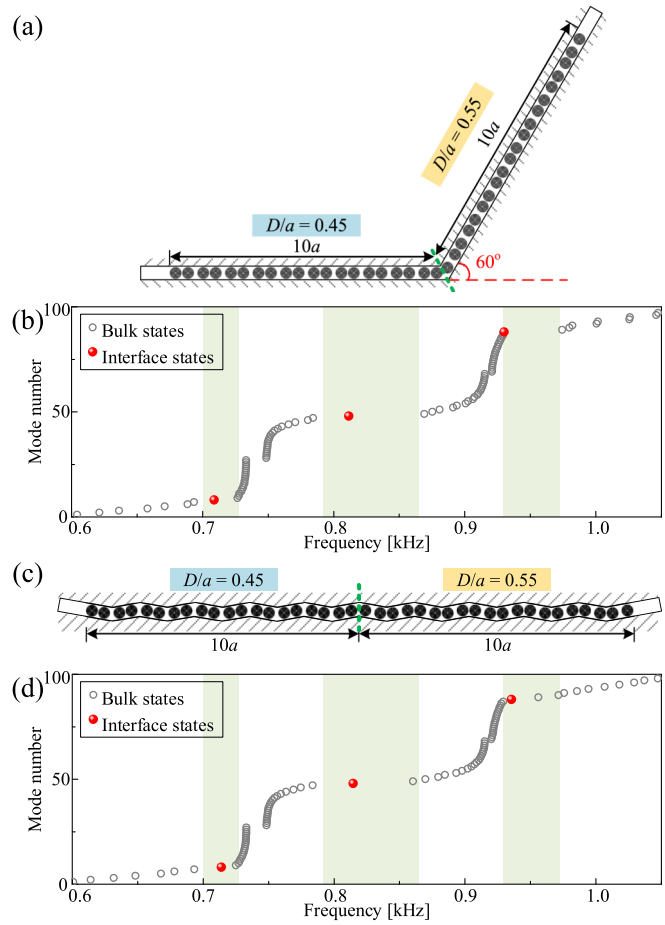

FIG. 14. (a) Rotating one-half of the PnC by 60°. (b) Eigenfrequency spectra of the 60°-bent PnC. (c)–(d) Same as (a)–(b), but arranging DMRs into a zigzagged waveguide.

APPENDIX H: ROBUSTNESS AGAINST THE SHAPE VARIATIONS OF THE WAVEGUIDE

In this section, we demonstrate that the designed topological interface state not only is robust against disordered DMRs but also remain resilient to perturbations of the waveguide. As shown in Fig. 13(a), a 10° bend has been introduced, leaving the topological interface states and the pressure as seen in Fig. 13(b) and Fig. 13(c), respectively, virtually unchanged.

Next, we increase the bend up to 60° as illustrated in Fig. 14(a) and do also reshape the waveguide into a zigzagged form as seen in Fig. 14(c). Surprisingly, apart from some marginal frequency shifts, the interface states as seen in Fig. 14(b) and Fig. 14(d) prevail rather identically.

[1] M. Z. Hasan and C. L. Kane, Rev. Mod. Phys. **82**, 3045 (2010).
[2] X.-L. Qi and S.-C. Zhang, Rev. Mod. Phys. **83**, 1057 (2011).
[3] F. D. M. Haldane and S. Raghu, Phys. Rev. Lett. **100**, 013904 (2008).
[4] Z. Wang, Y. D. Chong, J. D. Joannopoulos, and M. Soljačić, Phys. Rev. Lett. **100**, 013905 (2008).
[5] A. B. Khanikaev, S. H. Mousavi, W.-K. Tse, M. Kargarian, A. H. MacDonald, and G. Shvets, Nature Mater. **12**, 233 (2013).
[6] L. Lu, J. D. Joannopoulos, and M. Soljačić, Nature Photon. **8**, 821 (2014).
[7] A. B. Khanikaev and G. Shvets, Nature Photon. **11**, 763 (2017).
[8] Z. Yang, F. Gao, X. Shi, X. Lin, Z. Gao, Y. Chong, and B. Zhang, Phys. Rev. Lett. **114**, 114301 (2015).

[9] R. Fleury, A. B. Khanikaev, and A. Alu, Nature Commun. **7**, 11744 (2016).
[10] J. Mei, Z. Chen, and Y. Wu, Sci. Rep. **6**, 32752 (2016).
[11] Z. Zhang, Q. Wei, Y. Cheng, T. Zhang, D. Wu, and X. Liu, Phys. Rev. Lett. **118**, 084303 (2017).
[12] J. Lu, C. Qiu, L. Ye, X. Fan, M. Ke, F. Zhang, and Z. Liu, Nature Phys. **13**, 369 (2017).
[13] Z. Zhang, Y. Tian, Y. Cheng, X. Liu, and J. Christensen, Phys. Rev. B **96**, 241306(R) (2017).
[14] Z. Zhang, Y. Tian, Y. Cheng, Q. Wei, X. Liu, and J. Christensen, Phys. Rev. Appl. **9**, 034032 (2018).
[15] D. Zhao, M. Xiao, C. W. Ling, C. T. Chan, and K. H. Fung, Phys. Rev. B **98**, 014110 (2018).
[16] Z. Zhang, Y. Tian, Y. Wang, S. Gao, Y. Cheng, X. Liu, and J. Christensen, Adv. Mater. **30**, 1803229 (2018).
[17] H. He, C. Qiu, L. Ye, X. Cai, X. Fan, M. Ke, F. Zhang, and Z. Liu, Nature (London) **560**, 61 (2018).
[18] X. Zhang, M. Xiao, Y. Cheng, M.-H. Lu, and J. Christensen, Commun. Phys. **1**, 97 (2018).
[19] F. Zangeneh-Nejad and R. Fleury, Phys. Rev. Lett. **122**, 014301 (2019).
[20] Z. Zhang, M. Rosendol López, Y. Cheng, X. Liu, and J. Christensen, Phys. Rev. Lett. **122**, 195501 (2019).
[21] S. D. Huber, Nature Phys. **12**, 621 (2016).
[22] R. Chaunsali, C.-W. Chen, and J. Yang, Phys. Rev. B **97**, 054307 (2018).
[23] M. Miniaci, R. K. Pal, B. Morvan, and M. Ruzzene, Phys. Rev. X **8**, 031074 (2018).
[24] Q. Zhang, Y. Chen, K. Zhang, and G. Hu, Extreme Mech. Lett. **28**, 76 (2019).
[25] T.-W. Liu and F. Semperlotti, Phys. Rev. Appl. **11**, 014040 (2019).
[26] J. Zak, Phys. Rev. Lett. **62**, 2747 (1989).
[27] M. Xiao, Z. Q. Zhang, and C. T. Chan, Phys. Rev. X **4**, 021017 (2014).
[28] Y. Meng, H. Xiang, R.-Y. Zhang, X. Wu, D. Han, C. Chan, and W. Wen, Opt. Lett. **41**, 3698 (2016).
[29] M. Xiao, G. Ma, Z. Yang, P. Sheng, Z. Zhang, and C. T. Chan, Nature Phys. **11**, 240 (2015).
[30] Z. Yang and B. Zhang, Phys. Rev. Lett. **117**, 224301 (2016).
[31] X. Li, Y. Meng, X. Wu, S. Yan, Y. Huang, S. Wang, and W. Wen, Appl. Phys. Lett. **113**, 203501 (2018).
[32] Y. Meng, X. Wu, R.-Y. Zhang, X. Li, P. Hu, L. Ge, Y. Huang, H. Xiang, D. Han, S. Wang *et al.*, New J. Phys. **20**, 073032 (2018).
[33] R. Chaunsali, E. Kim, A. Thakkar, P. G. Kevrekidis, and J. Yang, Phys. Rev. Lett. **119**, 024301 (2017).
[34] S. A. Cummer, J. Christensen, and A. Alù, Nature Rev. Mater. **1**, 16001 (2016).
[35] V. M. García-Chocano, J. Christensen, and J. Sánchez-Dehesa, Phys. Rev. Lett. **112**, 144301 (2014).
[36] J. Christensen, A. Fernandez-Dominguez, F. de Leon-Perez, L. Martin-Moreno, and F. Garcia-Vidal, Nat. Phys. **3**, 851 (2007).
[37] K. Melde, A. G. Mark, T. Qiu, and P. Fischer, Nature (London) **537**, 518 (2016).
[38] Y. Tian, Q. Wei, Y. Cheng, and X. Liu, Appl. Phys. Lett. **110**, 191901 (2017).
[39] Y. Cheng, C. Zhou, B. Yuan, D. Wu, Q. Wei, and X. Liu, Nature Mater. **14**, 1013 (2015).
[40] J. Zhang, Y. Cheng, and X. Liu, Appl. Phys. Lett. **110**, 233502 (2017).
[41] H. Long, S. Gao, Y. Cheng, and X. Liu, Appl. Phys. Lett. **112**, 033507 (2018).
[42] S. Yves, R. Fleury, T. Berthelot, M. Fink, F. Lemoult, and G. Lerosey, Nature Commun. **8**, 16023 (2017).
[43] H.-X. Wang, G.-Y. Guo, and J.-H. Jiang, arXiv:1902.10401.